Accepted Manuscript

A coupled 3D isogeometric and discrete element approach for modelling interactions between structures and granular matters

Wei Gao, Jiaweng Wang, Shuohui Yin, Y.T. Feng

Please cite this article as: W. Gao, J. Wang, S. Yin et al., A coupled 3D isogeometric and discrete element approach for modelling interactions between structures and granular matters, *Computer Methods in Applied Mechanics and Engineering* (2019), https://doi.org/10.1016/j.cma.2019.05.043

A coupled 3D isogeometric and discrete element approach for modelling interactions between structures and granular matters

Wei GAO[a,*], Jiaweng WANG[a], Shuohui YIN[b,*], Y. T. FENG[c]

[a]*School of Electro-mechanical Engineering, Guangdong University of Technology, Guangzhou, China*
[b]*School of Mechanical Engineering, Xiangtan University, Hunan, China*
[c]*Zienkiewicz Centre for Computational Engineering, Swansea University, Swansea, UK*

Abstract

A three-dimensional (3D) isogeometric/discrete-element coupling method is presented for modelling contact/impact between structures and particles. This method takes advantages of the geometry smoothness and exactness of isogeometric analysis (IGA) for continuous solid media and the effectiveness and flexibility of the discrete element method (DEM) for particulate matters. The coupling procedure for handling interactions between IGA elements and discrete elements (DEs) includes global search, local search and interaction calculation. In the global search, the CGRID method is modified to detect potential contact pairs between IGA elements and DEs based on their bounding box representations. The strong convex hull property of a NURBS control mesh plays an important part in the bounding box representation of IGA elements. In the local search, the proposed approach treats each spherical DE centroid as a slave node and the contact surface of each IGA element as the master surface. The projection of a DE centroid onto an IGA element contact surface is solved by modifying the simplex method and Brent iterations. The contact force between an IGA element and a DE is determined from their penetration by using a (nonlinear) penalty function based method. The whole coupled system is solved by the explicit time integration within a updated Lagrangian scheme. Finally, three impact examples, including the

---

*Corresponding author: Wei GAO, Shuohui YIN

Email addresses: gaowei@gdut.edu.cn; hbweigao@126.com (Wei GAO), yinsh2016@163.com (Shuohui YIN)

impact of two symmetric bars, a tube onto a footing strip, and an assembly of granular particles to a tailor rolled blank, are simulated in elastic regime to assess the accuracy and applicability of the proposed method.

1. Introduction

Granular materials (GMs) play an important role in many engineering and industrial applications such as food processing, powder compaction, mineral processing, construction and renewable energy production. During processing and transporting of GMs, GM-structure interactions may have significant effects on structure wear, and even lead to possible structure failure, e.g. mill agitator wear, mixer ribbon or blade wear, conveyor wear, etc. At the same time, the interactions acting on GMs directly affect the flow, mixing processing and/or fracture behaviour of GMs [1].

The discrete element method (DEM) originally proposed by Cundall and Stack [2, 3] in the 1970s, is an effective numerical method to track the motion and flow of individual particles, and later has been extended to model continuous solid media and particularly the failure of brittle matters by bonding elements together [4]. However, in the context of DEM, structures interacting with particles are usually represented by rigid walls without considering their deformation [5], and hence the interaction between GMs and structures may not be taken into account accurately. The structure deformation can be analyzed by using the finite element method (FEM), which is the most commonly used numerical method for structure analysis. Therefore, some FE/DE coupling methods have been represented to deal with GM-structure interactions [6, 7, 8, 9, 10, 11, 12, 13, 14, 15, 16].

In traditional FEM, Lagrangian basis functions are used for the geometric description and the displacement-field approximation of structures [17]. This approach usually requires substantial efforts in mesh generation for complex geometries, leading to the non-smoothness at the common edges and/or nodes of adjacent surfaces, and also relatively low accurate geometric approximation. However, the interaction between GMs and structures is sensitive to the structure geometry, especially the interaction surface between the structures and GMs. Consequently, a higher precision geometric representation is preferable to more accurately calculate the interaction

2

force. Furthermore, the non-smoothness between FE surfaces usually leads to three types of DE/FE contact situations: DE-surface, DE-edge and DE-node. Some complicated approaches are developed to handle these contact situations approximately, such as several-plane-triangle or quadrangle equivalences [12, 13, 14] curved-surface equivalences [11, 15, 16]. In addition, the FE/DE contact force is prone to suffering the so-called discontinuity problem, especially when a DE is near FE edges and/or nodes [11, 18, 19], and may also lead to numerical instability due to the generation of superficial energy. A possible solution to this problem within the combined FE/DE framework involves using energy based contact theories [7, 20, 21].

A new computational method termed isogeometric analysis (IGA) was proposed by Hughes et al. [22] aiming at integrating FE meshes and computer-aided design (CAD) models. To achieve this purpose, IGA employs the same geometric basis functions as those describing geometries in CAD [23], e.g. B-spline or NURBS basis functions, to approximate the solution field. Therefore, CAD design models can be directly adopted for analysis in IGA without additional mesh generation. In addition, the analysis model in IGA is typically smooth, and almost the same as that in CAD, and thus the geometric approximation error is minimized. Because of these significantly advantages, which are considerably difficult to be achieved in traditional FEM, IGA has drawn numerous attentions in a variety of engineering applications, such as structural vibrations [24], plate and shell analysis [25, 26, 27], contact analysis [28], damage and fracture mechanics [29, 30], electromagnetic analysis [31], and fluid mechanics [32]. Moreover, IGA has shown more computational advantages than the standard FEM in fluid-structure and particle-structure interaction problems. Some novel coupling approaches have been developed, such as an isogeometric-meshfree coupling approach [33], a scaled boundary FEM-isogeometric coupling method [34], and an isogeometric-BEM (boundary element method) coupling approach [35].

In order to utilize the advantages of both IGA (the exact and smooth geometry and higher order approximation) and DEM (effectiveness for granular matters or simplicity for failure of brittle materials), it is desirable to couple IGA and DEM to simulate GM-structure interaction problems in one system. To the authors' best knowledge, no computational approach in terms of the coupled IGA/DEM framework has been proposed to model GM-structure interactions. This paper aims to develop such a coupling approach that utilizes two subdomains: the IGA subdomain for structure analysis and the DE subdomain for GMs or structural (using bonded DEs to represent) simulations.

3

The CGRID method [36, 37] is extended to detect the potential contact between IGA elements and DEs by using the strong convex hull property of the NURBS surface. Then, the contact position is determined via the combination of the Brent method [38, 39] and simplex iterations [40] for providing initial estimations. The contact force between the contact pair of a DE and an IGA element is computed by employed a penalty based method.

The paper is organized as follows. Section 2 introduces NURBS basis functions and isogeometric approximations. The basic formulations of discrete element models for both particulate systems and continuous solid media are briefly reviewed in Section 3. Section 4 describes the coupling approach and its algorithmic aspect based on a penalty function based method. Section 5 presents three numerical examples to assess the accuracy and applicability of the proposed coupling approach. Conclusions are drawn in Section 6.

2. Isogeometric method

2.1. NURBS basis functions

In order to construct NURBS basis functions, the knot vector $\boldsymbol{k}^I$ associated with the Ith dimension of a 3D surface patch is defined as

$$\boldsymbol{k}^I = \left\{ \underbrace{\xi_0^I, \ldots, \xi_{p_I}^I}_{(p_I+1)\text{terms}}, \xi_I^I, \ldots, \xi_i^I, \ldots, \xi_{n_I^k}^I, \underbrace{\xi_{n_I^k+1}^I, \ldots, \xi_{m_I^k}^I}_{(p_I+1)\text{terms}} \right\} \tag{1}$$

where ξ_i^I denotes the Ith knot. ξ^I is a nondecreasing sequence of real numbers, i.e. $\xi_i^I \leq \xi_{i+1}^I$, $i = 0, \ldots, t_I^k + p_I$. Also, $n_I^k + 1$ is the total number of the accompanying control nodes in the Ith dimension, and p_I denotes the degree of the accompanying B-spline basis functions. $m_I^k = n_I^k + n_I^e$, where $n_I^e = p_I + 1$ is the node number of each control mesh in the Ith direction. The non-zero knot spans $[\xi_i^1, \xi_{i+1}^1)$, $[\xi_j^2, \xi_{j+1}^2)$ and $[\xi_k^3, \xi_{k+1}^3)$ are defined as the parameter space for a 3D IGA element (i, j, k).

To determine the NURBS basis functions, the Ith B-spline basis function of degree p_I, $\phi_{i,p_I}(\xi^I)$, can be defined recursively as

$$\phi_{i,0}(\xi^I) = \begin{cases} 1, & \text{if } \xi_i^I \leq \xi^I < \xi_{i+1}^I \\ 0, & \text{otherwise} \end{cases} \tag{2}$$

and

$$\phi_{i,p_I}(\xi^I) = \frac{\xi^I - \xi_i^I}{\xi_{i+p_I}^I - \xi_i^I} \phi_{i,p_I-1}(\xi^I) + \frac{\xi_{i+p_I+1}^I - \xi^I}{\xi_{i+p_I+1}^I - \xi_{i+1}^I} \phi_{i+1,p_I-1}(\xi^I), \text{ for } p_I \geq 1 \tag{3}$$

4

When some repeating knots are involved in evaluating a basis function, which leads to a quotient of form $\Box/0$, the function is assigned to be zero. $\phi_{i,p_I}(\xi^I)$ is non-negative, and is referred to simply as $\phi_i(\xi^I)$ below for conciseness. $\phi_i(\xi^I)$ is infinitely differentiable in the interior of any non-zero knot span (ξ_i^I, ξ_{i+1}^I). At a knot ξ_i^I, however, $\phi_i(\xi^I)$ is $(p_I - k_I)$ times continuously differentiable, where k_I denotes the multiplicity of the knot. In any given knot span, at most p_I+1 of the basis shape functions $\phi_i(\xi^I)$ are not equal to zero, i.e. for the knot span $[\xi_i^I, \xi_{i+1}^I)$

$$\begin{cases} \phi_m(\xi^I) \neq 0, & \text{for } m = (i - p_I), \ldots, i \\ \phi_m(\xi^I) = 0, & \text{for } m < (i - p_I) \text{ or } m > i \end{cases} \tag{4}$$

The NURBS basis function $R_i(\xi^I)$ is represented by a weighted average of the B-spline basis functions as

$$R_i(\xi^I) = \frac{\phi_i(\xi^I)\omega_i}{\sum\limits_{m=0}^{n_I^k} \phi_m(\xi^I)\omega_m} \tag{5}$$

where ω_i is the ith weight. By applying Eq. (4), $R_i(\xi^I)$ in a given knot span $[\xi_i^I, \xi_{i+1}^I)$ can be rewritten as

$$R_i(\xi^I) = \frac{\phi_i(\xi^I)\omega_i}{\sum\limits_{m=i-p_I}^{i} \phi_m(\xi^I)\omega_m} \tag{6}$$

and in this knot span, only $R_{i-p_I}(\xi^I), \ldots, R_i(\xi^I)$ are not equal to zero.

By using the NURBS basis functions, a point in a NURBS solid element (i, j, k) can be parametrized as

$$\boldsymbol{V}_{ijk}(\xi^1, \xi^2, \xi^3) = \sum_{m=m_0}^{i} \sum_{n=n_0}^{j} \sum_{l=l_0}^{k} R_{mnl}(\xi^1, \xi^2, \xi^3)\boldsymbol{x}_{mnl} \tag{7}$$

where $m_0 = i - p_1$, $n_0 = j - p_2$, $l_0 = k - p_3$; $\boldsymbol{x}_{ijk}$ denotes the position vectors of the control nodes; and R_{ijk} is represented as

$$R_{ijk}(\xi^1, \xi^2, \xi^3) = \frac{\phi_i(\xi^1)\phi_j(\xi^2)\phi_k(\xi^3)\omega_{ijk}}{\sum\limits_{m=m_0}^{i} \sum\limits_{n=n_0}^{j} \sum\limits_{l=l_0}^{k} \phi_m(\xi^1)\phi_n(\xi^2)\phi_l(\xi^3)\omega_{mnl}}. \tag{8}$$

5

By inheriting the geometric parameters from the NURBS volume, a NURBS surface patch can be fully determined [41] by setting $\xi^3 = 0$ or 1. For instance, by substituting $\xi^3 = 1$ and Eq. (8) into Eq. (7), the (upper) surface of the NURBS element (i, j, k) at $\xi^3 = 1$ can be expressed as

$$\boldsymbol{S}_{ij}(\xi^1, \xi^2) = \sum_{m=m_0}^{i} \sum_{n=n_0}^{j} R_{mn}(\xi^1, \xi^2)\boldsymbol{x}_{mn} \tag{9}$$

where $\boldsymbol{x}_{mn}$ are the position vectors of the control nodes for the surface $\xi^3 = 1$ and

$$R_{mn}(\xi^1, \xi^2) = \frac{\phi_m(\xi^1)\phi_n(\xi^2)\omega_{mn}}{\displaystyle\sum_{M=m_0}^{i} \sum_{N=n_0}^{j} \phi_M(\xi^1)\phi_N(\xi^2)\omega_{MN}} \tag{10}$$

in which $R_{mn}(\xi^1, \xi^2)$ denotes the NURBS surface shape function of the control node (m, n) that is located at the mth position in the ξ^1 direction and the nth position in the ξ^2 direction; ω_{mn} is the weighting factor of the control node on the element surface $\xi^3 = 1$. In order to calculate the projection of a point on the NURBS surface (see Section 4.2), the derivatives of the NURBS surface with $\xi^3 = 1$ can be determined as

$$\frac{\partial \boldsymbol{S}_{ij}(\xi^1, \xi^2)}{\partial \xi_I} = \sum_{m=m_0}^{i} \sum_{n=n_0}^{j} \frac{\partial R_{mn}(\xi^1, \xi^2)}{\partial \xi_I}\boldsymbol{x}_{mn} \quad (I = 1, 2) \tag{11}$$

with

$$\frac{\partial R_{mn}(\xi^1, \xi^2)}{\partial \xi_I} = \frac{\omega_{mn}\partial[\phi_m(\xi^1)\phi_n(\xi^2)]/\partial\xi^I - R_{mn}(\xi^1, \xi^2)\partial\omega/\partial\xi^I}{\omega} \tag{12}$$

where ω is represented as

$$\omega = \sum_{m=m_0}^{i} \sum_{n=n_0}^{j} \phi_m(\xi^1)\phi_n(\xi^2)\omega_{mn} \tag{13}$$

2.2. The weak form of the governing equations in IGA

For a single IGA element, the weak form of the governing equations can be expressed as

$$\boldsymbol{M}_{\mathrm{e}}\ddot{\boldsymbol{u}}_{\mathrm{e}} = \boldsymbol{f}_{\mathrm{e}}^{\mathrm{ext}} - \boldsymbol{f}_{\mathrm{e}}^{\mathrm{int}} \tag{14}$$

6

where $\boldsymbol{u}_e$ is the nodal displacement vector of the element; $\ddot{\boldsymbol{u}}_e$ is the acceleration vector; $\boldsymbol{f}_e^{\text{ext}}$ denotes the external nodal force vector; and $\boldsymbol{f}_e^{\text{int}}$ is the internal nodal force vector given by

$$\boldsymbol{f}_e^{\text{int}} = \int_{V_e} \boldsymbol{B}^{\text{T}} \boldsymbol{\sigma} \mathrm{d}V \tag{15}$$

where $\boldsymbol{\sigma} = [\sigma_{11}, \sigma_{22}, \sigma_{33}, \sigma_{23}, \sigma_{13}, \sigma_{12}]$ is the Voigt notation representation of the stress tensor; and the strain matrix $\boldsymbol{B}$ can be rewritten as

$$\boldsymbol{B} = [\boldsymbol{B}_1, \boldsymbol{B}_2, \ldots, \boldsymbol{B}_I, \ldots, \boldsymbol{B}_N], \quad N = (p_1 + 1)(p_2 + 1)(p_3 + 1) \tag{16}$$

in which $\boldsymbol{B}_I$ is represented as

$$\boldsymbol{B}_I = \begin{bmatrix} \frac{\partial R_I}{\partial x_1} & 0 & 0 & 0 & \frac{\partial R_I}{\partial x_3} & \frac{\partial R_I}{\partial x_2} \\ 0 & \frac{\partial R_I}{\partial x_2} & 0 & \frac{\partial R_I}{\partial x_3} & 0 & \frac{\partial R_I}{\partial x_1} \\ 0 & 0 & \frac{\partial R_I}{\partial x_3} & \frac{\partial R_I}{\partial x_2} & \frac{\partial R_I}{\partial x_1} & 0 \end{bmatrix}^{\text{T}} \tag{17}$$

where R_I is equal to R_{ijk} and $I = i \times j \times k$.

3. Discrete element models

Both contact models and bonded models are commonly used in the spherical discrete element method. Various contact models have a wide range of applications to handle the interaction of granular materials [42, 43]. Bonded models are usually employed to analyze the deformation of brittle materials, e.g. glass, rock and concrete [44, 45]. To simulate the fracture process of brittle materials, the bonded model can be switched to the contact model when the failure criterion is satisfied [4, 46]. The switch between these two models and the simulation of fracture processes are not considered in our present work as it focuses on the couping between IGA and DEM.

3.1. Contact model for spherical elements

Only spherical discrete elements are considered and no friction force will be taken into account in the present work. When two spheres i and j are in contact, as shown in Fig. 1, a contact model based on the Hertz-Mindlin theory is used to calculate the contact force. The contact force in this model is usually divided into normal and tangential contact components. The normal
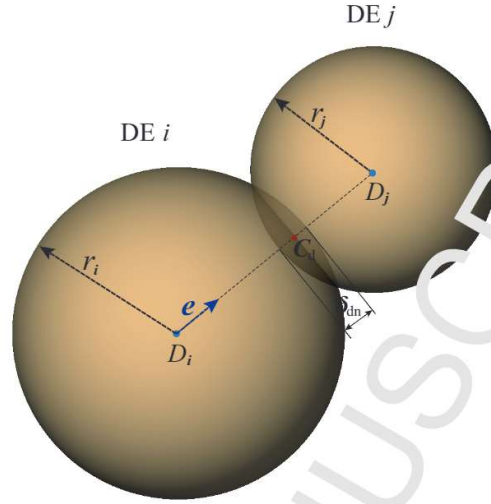
7

Figure 1: Two discrete elements in contact

contact force $\boldsymbol{f}_{\mathrm{dn}}$ for the element i can be calculated based on the Hertz model [47] as

$$\boldsymbol{f}_{\mathrm{dn}} = \frac{4}{3}E^*(r^*\|\boldsymbol{\delta}_{\mathrm{dn}}\|^{1/2})\boldsymbol{\delta}_{\mathrm{dn}} \tag{18}$$

where $\boldsymbol{\delta}_{\mathrm{dn}}$ are the overlap vector determined by

$$\boldsymbol{\delta}_{\mathrm{dn}} = (r_i + r_j - \|\boldsymbol{d}_i - \boldsymbol{d}_j\|)\boldsymbol{e} \tag{19}$$

in which $\boldsymbol{e} = (\boldsymbol{d}_i - \boldsymbol{d}_j)/(\|\boldsymbol{d}_i - \boldsymbol{d}_j\|)$ is a unit vector through the DE centroids; and r_i and r_j are the radii of DEs i and j respectively. The equivalent radius r^* and Young's modulus E^* are defined as

$$r^* = \frac{r_i r_j}{r_i + r_j}, \tag{20}$$

$$E^* = \frac{E_i E_j}{(1 - \nu_i^2)E_j + (1 - \nu_j^2)E_i} \tag{21}$$

where E_i and E_j are the Young's moduli of the two DEs, and ν_i and ν_j denote their Poisson's ratios.

The tangential contact force $\boldsymbol{f}_{\mathrm{ds}}$ for DE i can be determined based on the Mindlin theory as

$$\boldsymbol{f}_{\mathrm{ds}} = \frac{16}{3}G^*(r^*|\boldsymbol{\delta}_{\mathrm{dn}}|)^{1/2}\boldsymbol{\delta}_{\mathrm{ds}}. \tag{22}$$

8

Here G^* and $\boldsymbol{\delta}_{\mathrm{ds}}$ are the equivalent shear modulus and tangential relative displace respectively, which are defined as

$$G^* = \frac{G_i G_j}{(2 - \nu_i)G_j + (2 - \nu_j)G_i}, \tag{23}$$

$$\boldsymbol{\delta}_{\mathrm{ds}} = \int_{t_1}^{t_2} \boldsymbol{v}_{\mathrm{s}}' \mathrm{d}t \tag{24}$$

where G_i and G_j are the DE shear moduli; $\boldsymbol{v}_{\mathrm{s}}'$ is the relative velocity at the contact point C_{d}; and $[t_1, t_2]$ is the contact time interval.
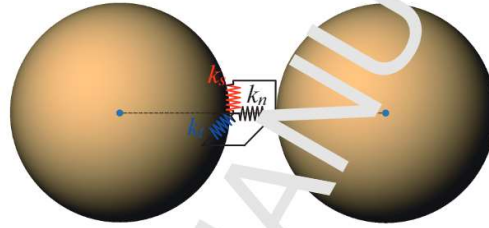
3.2. Bonded model

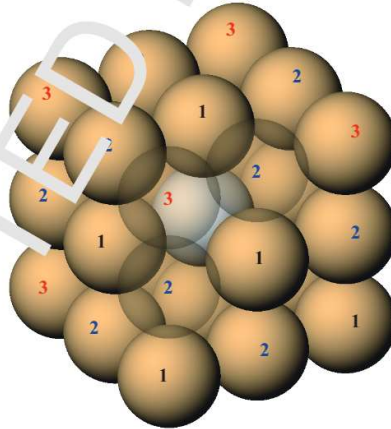Figure 2: Springs connecting two discrete elements

Figure 3: A cubic arranged bonded discrete element model

The bonded model is relatively simple in which two neighbouring spherical elements are connected by a beam, or by one normal spring and two

9

tangential springs, as shown in Fig. 2. In this model, the spring stiffnesses are usually related to the DE arrangement. Several bonded models with different arrangements have been reported in the literature [48, 49, 50]. Because the cubic arranged DE model is prone to describing the geometry more accurately, this particular bonded DE model is employed in this paper for simplicity, as shown in Fig. 3.

In this bonding configuration, the central gray element is connected with twenty-six neighboring orange elements by springs. Because of the symmetry of the packing, the connections between the central element and its neighbors can be classified into three types and are marked by numbers 1, 2 and 3 on the neighboring elements, as shown in Fig. 3. Based on the energy equivalence principle, i.e. the total elastic energy stored in the springs in a certain domain is equal to the strain energy stored by the elastic solid in the same domain, the spring stiffnesses for the three connection types are found to be [51]

$$k_{\mathrm{n}}^1 = \frac{2Er\nu}{(1-2\nu)(1+\nu)} \tag{25}$$

$$k_{\mathrm{n}}^2 = \frac{Er}{2(1-2\nu)(1+\nu)} \tag{26}$$

$$k_{\mathrm{s}}^2 = k_{\mathrm{t}} = \frac{Er(1-4\nu)}{2(1-2\nu)(1+\nu)} \tag{27}$$

$$k_{\mathrm{s}}^1 = k_{\mathrm{t}}^1 = k_{\mathrm{n}}^3 = k_{\mathrm{s}}^3 = k_{\mathrm{t}}^3 = 0 \tag{28}$$

where k_{n} and k_{s} denote the normal and tangential spring stiffnesses, respectively; $k_{\square}^i$ means spring stiffness for type i connection ($i = 1, 2, 3$); and E and ν are the Young's modulus and Poisson's ratio of the solid, respectively.

4. Coupling approach

4.1. Global search

The purpose of the global search is to detect potential or candidate contact pairs between a NURBS surface or its control mesh and discrete elements based on their bounding box representations. The key to this step is to utilize the strong convex hull property of a NURBS surface, i.e. *a NURBS surface is fully enclosed in the convex hull of its control nodes*, and thus to use the bounding box of its control nodes of a NURBS for the global search.

To illustrate this strong convex hull property of a NURBS more clearly, a two-dimensional (2D) second-degree NURBS curve is shown in Fig. 4, where

10

N_i denotes the ith control node; C_i is the ith section of the second-degree NURBS curve; H_3 is the third convex hull, i.e. control triangle. It is clear, for instance, that the triangle H_3 contains the curve C_3.
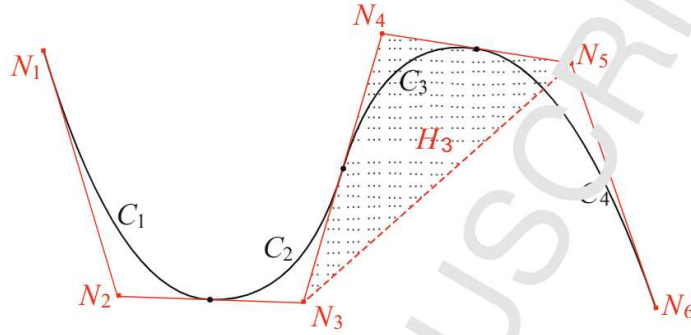
Figure 4: The convex hull contains the corresponding second-degree NURBS curve (degree $p_1 = 2$, node number of a control polygon $n_1^{\mathrm{e}} = v_1 + 1 = 3$)
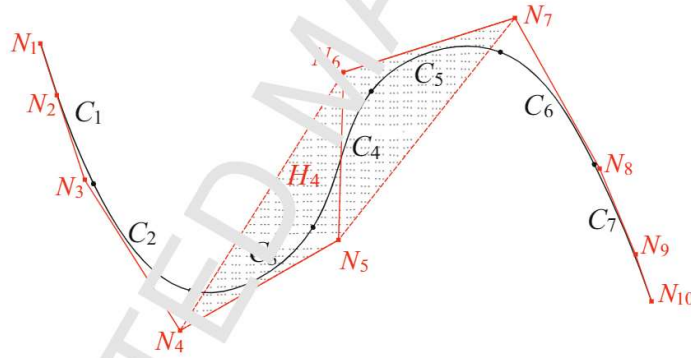
Figure 5: The convex hull contains a section of a third-degree NURBS curve ($p_1 = 3$, $n_1^{\mathrm{e}} = 4$)

Note that the convex hull instead of the control mesh contains the corresponding curve section. Fig. 5 shows a third-degree NURBS curve with $p_1 = 3$, $n_1 = 4$). In this figure, the control mesh and the curve are both concave, and the curve section C_4 is not inside the control mesh $N_4N_5N_6N_7$, but inside the convex hull H_4, i.e. polygon $N_4N_5N_7N_6$. Hence, when a DE overlaps the convex hull of a control mesh, this DE has the possibility to be in contact with the corresponding NURBS section of the control mesh.

11

In this paper, the CGRID search method [21, 36] is extended to detect overlapping convex hulls of IGAs and DEs by representing both convex hulls and DEs as axis aligned bounding boxes (AABB).

It is worth noting that a convex hull has the same control nodes as its control mesh, and thus it is unnecessary to distinguish a convex hull and its control mesh when generating AABBs. The detected potential contact pairs, the DEs and the corresponding control meshes, are stored for the next local search stage to be described in Section 4.2.

Since the global search for a problem involving a large number of DEs is often time-consuming, it is desirable not to perform this process at every time step, but only when necessary. This is achieved by extending both DE radii and NURBS surfaces by (small) buffer zones so that the corresponding AABBs are also enlarged. Thus, as long as both the DE and the control mesh of a contact pair are fully enclosed by their extended AABBs in the subsequent time steps, the contact pair is still valid and a new search is not necessary. A new global search only needs to be conducted at a time instance when any contact pair is no longer valid. See [52] for more detail about using the buffer zone for the global search. Because a much smaller deformation is expected for NURBS surfaces than DEs, a smaller buffer zone is used for a NURBS than those buffer zones for DEs.

Generally speaking, the larger the DE radii/NURBS are extended, the lesser frequent the global search needs to be performed, thereby reducing the associated costs. However, more potential candidate contact pairs are likely to be detected. Consequently, in the local search stage more calculations needs to be involved to exclude those non-overlapping contact pairs, leading to the increased costs in this local search stage. Therefore an optimal overall performance for the contact detection including both global and local searches may be achieved by properly selecting the sizes of buffer zones used on the basis of the (relative) velocities of DEs and NURBS concerned.

4.2. Local search

Since potential candidate contact pairs between NURBS surfaces and DEs have been identified in the global search stage, the actual contact situations between these contact pairs can be further determined in the local search stage. It is computationally expensive to determine whether a DE is in contact with an IGA element or not, as will be described below, the convex hull of an IGA element is first replaced by the corresponding Oriented Bounding Box (OBB), and then a local contact resolution is conducted between the

12

OBB with the sphere of the DE. This will exclude those contact pairs where the DE is not in actual overlap with the OBB due to the better compactness of the OBB representation than that of the AABB, and therefore will reduce the computational cost involved in the local search. For clarity, Fig. 6 illustrates both AABB and OBB of the convex hull H_3 of the NURBS curve displayed in Fig. 4.
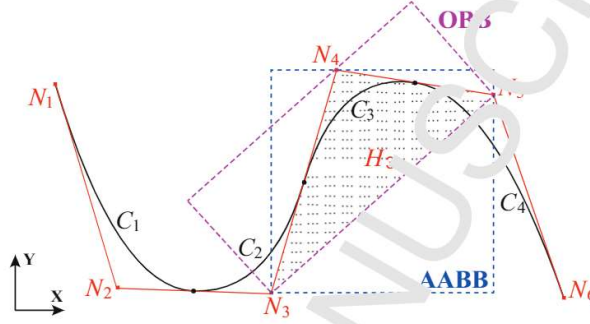

Figure 6: The AABB and OBB of the convex hull H_3

In isogeometric analysis, existing local contact methods can be mainly divided into three types: the node-to-surface (NTS) method [53], the Gauss-point-to-surface (GPTS) method [11, 54, 55] and the Mortar method [56, 57, 58]. Because the particulate nature of GMs that are simulated by DEM, the so-called NTS method is employed in the local search for IGA/DEM contact.

A possible contact situation between a NURBS surface and a sphere is shown in Fig. 7, in which D denotes the centre of the DE, and C is the closest projection of D on the NURBS surface. Note that D can be viewed as a slave node in the NTS method. Let $\boldsymbol{d}$ and $\boldsymbol{x}$ be the position vectors of D and C, respectively.

To find the closest projection C, i.e. $\boldsymbol{x}(\xi_c^1, \xi_c^2)$, the following equations need to be solved simultaneously

$$\frac{\partial \boldsymbol{x}}{\partial \xi^1}\big|_{(\xi_c^1, \xi_c^2)} \cdot [\boldsymbol{d} - \boldsymbol{x}(\xi_c^1, \xi_c^2)] = 0 \tag{29}$$

$$\frac{\partial \boldsymbol{x}}{\partial \xi^2}\big|_{(\xi_c^1, \xi_c^2)} \cdot [\boldsymbol{d} - \boldsymbol{x}(\xi_c^1, \xi_c^2)] = 0 \tag{30}$$

where ξ_c^1 and ξ_c^2 are the unknown values of the parameter coordinates at the projection on the NURBS surface.
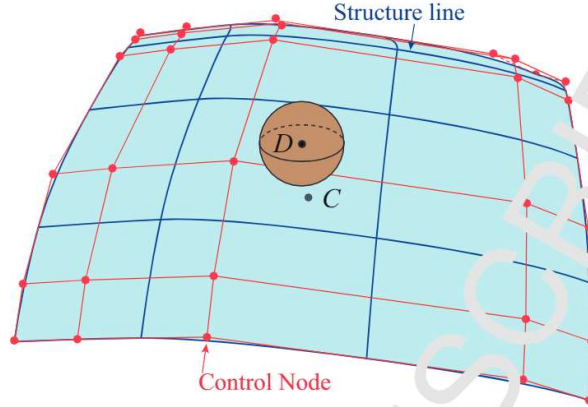
13

Figure 7: The projection of a DE centroid on the NURBS surface

The Brent iteration method [38, 39] is employed to solve Eqs. (29) and (30) simultaneously. Because of its local convergence, the initial values of $\xi_{\rm c}^1$ and $\xi_{\rm c}^2$ need to be estimated by a robust approach. Since only the squared distance function $s_{\rm d} = \|\boldsymbol{d} - \boldsymbol{x}(\xi_{\rm c}^1, \xi_{\rm c}^2)\|^2$ is needed, not its derivatives [40, 59], the simplex method is considered to be a robust unconstrained optimization method, and thus is employed for the initial value estimation of the Brent iteration.

In the simplex method, the minimal function value is approximatively obtained by mirroring and/or shrinking triangles in the parameter space [40]. Specifically, a vertex with the maximal $s_{\rm d}$ is identified from the three vertices of a triangle. Then a new triangle is formed by mirroring this vertex along its opposite side, as shown in Fig. 8. If the mirrored vertex still has the maximal $s_{\rm d}$ among the vertices of the new triangle, the vertex with the second largest $s_{\rm d}$ will be mirrored next to avoid a runaway loop. Besides, it is worth noting that one vertex may stay in a position without movement for c iterations, which suggests that the triangle may just rotate around this vertex in these iterations. In this situation, the triangle will be scaled down, e.g. by half. In 2D cases, the iteration number c is advisably set to be five.

In this paper, the initial parameter coordinates of the vertices of the start triangle are determined as

$$\boldsymbol{V}_0^1 = (\xi_{\rm c,0}^1, \xi_{\rm c,0}^2), \ \boldsymbol{V}_0^2 = (\xi_{\rm c,0}^1 + \alpha p, \xi_{\rm c,0}^2 + \alpha q), \ \boldsymbol{V}_0^3 = (\xi_{\rm c,0}^1 + \alpha q, \xi_{\rm c,0}^2 + \alpha p) \quad (31)$$

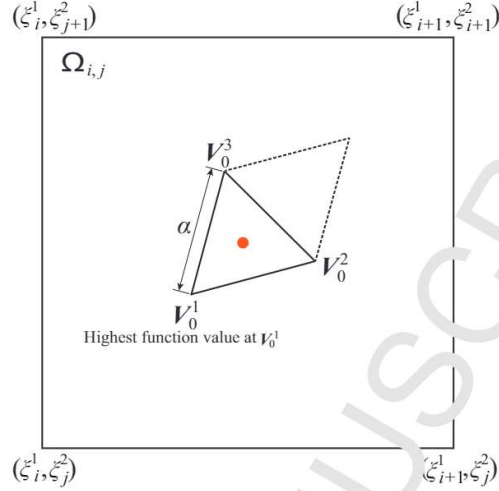where $p = (\sqrt{3} + 1)/(2\sqrt{2})$, $q = (\sqrt{3} - 1)/(2\sqrt{2})$; the initial length of the

14

Figure 8: The initial triangle and the mirrored one in the parameter domain of surface (i,j), i.e. $\Omega_{i,j}$

simplex edge α is set as

$$\alpha = \min(L_i^1/N, L_j^2/N) \tag{32}$$

where N can be set to a value in the interval $[5, 10]$. The centroid of the initial triangle is assumed to coincide with that of the parameter rectangle of the surface (i,j), as shown in Fig. 8, and thus $\xi_{c,0}^1$ and $\xi_{c,0}^2$ are determined as

$$\boldsymbol{\xi}_{c,0} = \left(\begin{array}{c} \xi_{c,0}^1 \\ \xi_{c,0}^2 \end{array} \right) = \frac{1}{2} \left(\begin{array}{c} \xi_i^1 + \xi_{i+1}^1 \\ \xi_j^2 + \xi_{j+1}^2 \end{array} \right) - \frac{\alpha}{\sqrt{6}}. \tag{33}$$

During the iterations of the simplex and Brent methods, the parameter values obtained for the surface (i,j) may occasionally be out of the parameter domain $\Omega_{i,j} = [\xi_i^1, \xi_{i+1}^1] \times [\xi_j^2, \xi_{j+1}^2]$, and then return again. Hence, the parameter solution domain for the surface is extended as

$$\xi_c^1 \in [\xi_i^1 - \beta L_{i-1}^1, \xi_{i+1}^1 + \beta L_{i+1}^1] \tag{34}$$

$$\xi_c^2 \in [\xi_j^2 - \beta L_{j-1}^2, \xi_{j+1}^2 + \beta L_{j+1}^2] \tag{35}$$

where $\beta \in (0,1)$ denotes the buffer factor, and the corresponding extended domain is denoted as $\Omega_{i,j}^e$.

15

If the parameter values in the iteration process are outside the domain $\Omega^e_{i,j}$ described by Eqs. (34) and (35), they will be assumed not to return back to the domain again. Consequently, the DE is assumed to be not in contact with this IGA element. When the parameters are located in the domain $\Omega^e_{i,j}$, in order to calculate the shape function values, it is necessary to determine which subdomain that the parameters belong to. Hence, four intermediate values χ_1 and χ_4 are defined as

$$\chi_1 = \xi^1_c - \xi^1_i, \quad \chi_2 = \xi^1_c - \xi^1_{i+1}, \quad \chi_3 = \xi^2_c - \xi^2_j, \quad \chi_4 = \xi^2_c - \xi^2_{j+1} \qquad (36)$$

By the sign combinations from χ_1 to χ_4, we can determine which subdomain (i.e. its surface index) where the parameters ξ^1_c, ξ^2_c are located, as shown in Fig. 9. Note that signs in round brackets mean that these signs are unnecessary to be computed when determining the subdomain. For instance, if the sign combination from χ_1 to χ_4 is computed as $+(-) - (-)$, the subdomain that the parameters lie in can be determined as $\Omega_{i,j-1}$. When the subdomain is determined, the corresponding shape-function values can be calculated by using Eq. (10).

Once the shape-function values at the projection point are calculated, the projection of the DE centroid on the NURBS surface can be determined from the position vectors of the corresponding control nodes. Because only the shape-function values of the surface's control nodes are nonzero, the position vector of the projected point $\boldsymbol{x}_c = \boldsymbol{x}(\xi^1_c, \xi^2_c)$ on surface (i,j) can be calculated as

$$\boldsymbol{x}_c = \sum_{m=m_0}^{i} \sum_{n=n_0}^{j} R_{mn}(\xi^1_c, \xi^2_c)\boldsymbol{x}_{mn}; \; m_0 = i - p_1, \ldots, i; n_0 = j - p_2, \ldots, j \qquad (37)$$

where m and n denote, respectively, the mth and n^{th} control nodes of the patch in both ξ^1 and ξ^2 directions; $R_{mn}(\xi^1_c, \xi^2_c)$ denotes the shape-function value at the projection; and $\boldsymbol{x}_{mn}$ is the position vector of the control node.

Because the penetration between a DE and a NURBS surface is generally small in comparison with the DE radius, the DE centroid is assumed always to be outside IGA elements. Hence, we can characterize the relative position of a DE and a NURBS surface by the penetration vector $\boldsymbol{\delta}$

$$\boldsymbol{\delta} = \begin{cases} (r - |\boldsymbol{x}_d - \boldsymbol{x}_c|)\boldsymbol{n}, & r - |\boldsymbol{x}_d - \boldsymbol{x}_c| > 0 \\ \boldsymbol{0}, & \text{otherwise} \end{cases} \qquad (38)$$

16
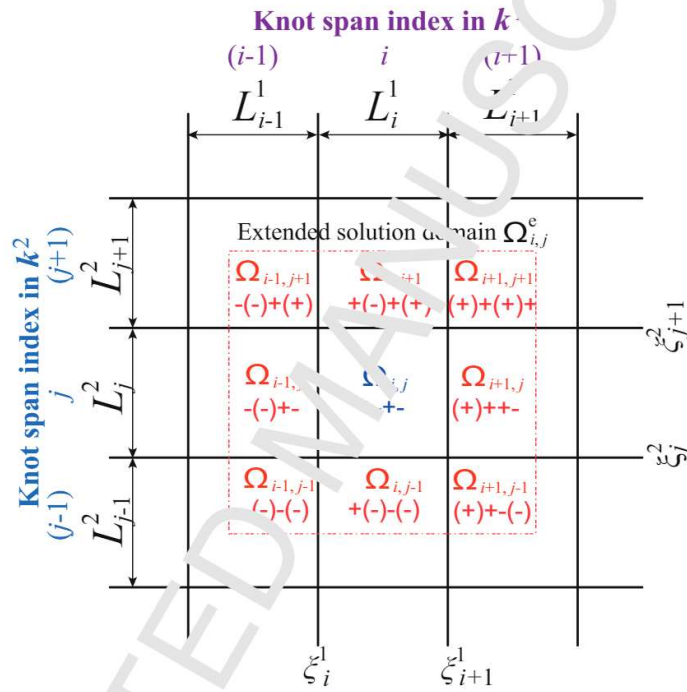
Figure 9: The extended parameter solution domain and the sign combinations from χ_1 to χ_4 in subdomains

17

where $\boldsymbol{n} = (\boldsymbol{x}_\mathrm{d} - \boldsymbol{x}_\mathrm{c})/\|\boldsymbol{x}_\mathrm{d} - \boldsymbol{x}_\mathrm{c}\|$ denotes the unit normal vector at the projection; and r is the radius of the DE.

The central difference method, as an explicit method, is employed for the subsequent time integration of the whole system, and its critical time step is usually very small. Within such a small time interval, the projection generally shifts slightly on the NURBS surface, and thus it is advisable to set the initial parameter values of the Brent method in the current time step from the converged value from the last time step. By adopting this initial guess, the Brent method usually converges in five iterations or less. As a result, for a certain contact pair, it is unnecessary to preform the simplex iteration at every time step.

4.3. Contact force

After the projection of a DE centroid on a NURBS surface and their penetration vector have been computed in the local search stage, the contact force between the DE and the IGA element can be calculated.

In the present work, a penalty function method is employed to determine the contact force based on the Hertz model. The curvature radius of the NURBS surface at the contact point is usually much larger than the DE radius, and thus the equivalent r^* is approximated to be the DE radius r. Hence, the contact force between a DE and an IGA element can be calculated based on Eq. (18) as

$$\boldsymbol{f} = \gamma E_c(r\|\boldsymbol{\delta}\|)^{1/2}\boldsymbol{\delta} \tag{39}$$

where E_c is the nominal Young's modulus for contact calculated from the material properties of both contacting IGA and DEM domains, and γ is a user-specified penalty factor. A proper estimation of this penalty factor is needed to prevent a large penetration but more importantly to obtain an accurate solution. This issue will be further discussed in numerical examples presented in Section 5.

Because the penetration vector $\boldsymbol{\delta}$ points to the DE centroid, the contact force $\boldsymbol{f}$ acts on the DE centroid without generating a torque. The reciprocal reaction force acting on the IGA element can be distributed to the corresponding control nodes by using the nodal shape functions. Because only the control nodes of the contact surface have nonzero shape-function values, the contact force should only be distributed to these control nodes, and the corresponding distributed contact forces $\boldsymbol{f}_{mn}$ are given by

$$\boldsymbol{f}_{mn} = -R_{mn}(\xi_\mathrm{c}^1, \xi_\mathrm{c}^2)\boldsymbol{f} \tag{40}$$

18

where $R_{mn}(\xi_c^1, \xi_c^2)$ is the shape-function value at the contact point for the control node at the mth and n^{th} positions along the ξ^1 and ξ^2 directions respectively.

4.4. Implementation

Based on the above proposed IGA/DEM coupling method, a 3D numerical analysis program CIGADEM is developed. An explicit time integration, i.e. a central difference method, and an updated Lagrangian formulation are employed. The program implementation flow chart is described in Fig. 10.

The whole procedure mainly contains several crucial steps: (1) IGA/DEM global search when needed, (2) IGA/DEM contact coupling, (3) IGA element internal force calculation, (4) DEM contact and connective force calculations, (5) external force computations, (6) kinetic variables update (solution step), and (7) displacement boundary imposition and etc. Note that steps (2)-(5) can be implemented in an arbitrary order and can be simultaneously executed in a parallel computing environment.
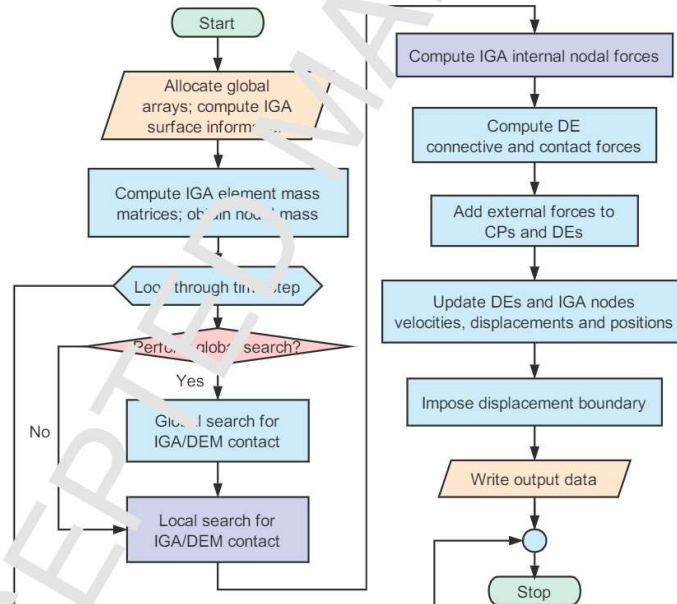
Figure 10: Implementation flow chart

The procedure for the IGA element internal force calculation is depicted in Fig. 11. In this procedure, the Cauchy stress rate tensor $\dot{\boldsymbol{\sigma}}$ is employed,

19

which is determined as

$$\dot{\boldsymbol{\sigma}} = \boldsymbol{\sigma}^{\nabla} + \boldsymbol{\sigma} \cdot \boldsymbol{W}^{T} + \boldsymbol{W} \cdot \boldsymbol{\sigma} \tag{41}$$

where $\boldsymbol{W}$ is a spin tensor; and $\boldsymbol{\sigma}^{\nabla}$ is the Jaumann stress rate tensor. The Cauchy stress tensor at time $t + \Delta t$, i.e. $\boldsymbol{\sigma}(t + \Delta t)$, can be updated from that of the previous time step as

$$\boldsymbol{\sigma}(t + \Delta t) = \boldsymbol{\sigma}(t) + \dot{\boldsymbol{\sigma}}\left(t + \frac{\Delta t}{2}\right)\Delta t \tag{42}$$
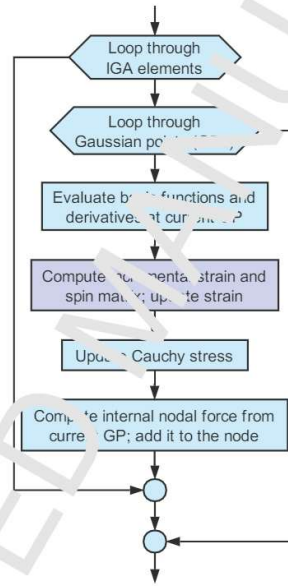
Here, Δt denotes the current time step.

Figure 11: IGA nodal internal force calculation procedure

In the CIGADEM program, the simplex algorithm [40] is modified to evaluate the initial parameter values of the Brent iteration, and the implementation of the IGA/DEM contact method is described in Table 1.

The notation $\square_{mn}$, e.g. R_{mn}, $\boldsymbol{f}_{mn}$, is used for conciseness and easy understanding. In the program implementation, however, the control node indices are read as input data and stored for each IGA element via one-dimensional (1D) array. Therefore, $\square_{mn}$ is also stored in a 1D array having the corresponding elements as those of the control node index array.

20

Table 1: The algorithm of the local search and contact force calculation

loop over contact surfaces of IGA elements

    1. obtain the detail of current surface and its 8 neighbor ones (see Figure 9)

    2. obtain surface index $P_{\mathrm{id}} = (i, j)$

    3. compute parameter solution space Ω_{ij}^{e}

    loop over potential contact DEs for the current surface

        1. obtain DE datum, e.g. $\boldsymbol{d}$, r, E, μ, etc.

        2. initialize contact-state flag, cFlag $= 0$

        3. initialize $m_{\mathrm{old}}^{\mathrm{x}} = -1$, $m_{\mathrm{old}}^{\mathrm{n}} = -1$, $P_{\mathrm{id}}^{h} = P_{\mathrm{id}}$

        4. initialize center and vertex coordinates $\boldsymbol{\xi}_{\mathrm{c},0}$, $\boldsymbol{V}_j$

        for $k = 1, 2, \cdots, k_{\max}$ for minimal S_{d}

          (a) **if**($\boldsymbol{V}_k^1$, $\boldsymbol{V}_k^2$ or $\boldsymbol{V}_k^3 \notin \Omega_{ij}^{\mathrm{e}}$)**then exit**;

          (b) update surface index P_{id}^{h} where $\boldsymbol{V}_k^h$ lie;

          (b) compute $R_{mn}(\xi_{\mathrm{c},k}^1, \xi_{\mathrm{c},k}^2)$ at $\boldsymbol{V}^1$, $\boldsymbol{V}^2$ and $\boldsymbol{V}_k^3$ on surface P_{id}^{h}

          (c) compute S_{d} at these vertices

          (d) find vertex indices m_{x}, m_{c} and m_{n} with maximal,

            medium and minimal S_{d}, respectively

          (e) **if**($m_{\mathrm{x}} = m_{\mathrm{old}}^{\mathrm{x}}$)**then** $m_{\mathrm{r}} = m_{\mathrm{c}}$ **else** $m_{\mathrm{r}} = m_{\mathrm{x}}$

          (f) $m_{\mathrm{old}}^{\mathrm{x}} = m_{\mathrm{r}}$

          (g) **if**($m_{\mathrm{n}} = m_{\mathrm{old}}^{\mathrm{n}}$)**then** $c = c + 1$

          else $m_{\mathrm{old}}^{\mathrm{n}} = m_{\mathrm{n}}$; $c = 0$

          (h) **if**($c > 5$)**then** $\boldsymbol{V}_k^j = \boldsymbol{V}_k^h + 0.5(\boldsymbol{V}_{m_{\mathrm{n}}}^h - \boldsymbol{V}_k^h)$, $j \neq m_{\mathrm{n}}$;

          (i) $\boldsymbol{V}_k^{\mathrm{s}} = 0.5 \sum_{h, \neq m_{\mathrm{r}}}^3 \boldsymbol{V}_k^h$

          (j) $\boldsymbol{V}_k^{m_{\mathrm{r}}} = \boldsymbol{V}_k^{\mathrm{s}} + (\boldsymbol{V}_k^{\mathrm{s}} - \boldsymbol{V}_k^{m_{\mathrm{r}}})$

          (k) $\boldsymbol{\xi}_{\mathrm{c},k+1} = \frac{1}{3} \sum_{h=1}^3 \boldsymbol{V}_k$

          (l) **if**($\|\boldsymbol{\xi}_{\mathrm{c},k+1} - \boldsymbol{\xi}_{\mathrm{c},k}\| \leq$ tol)**then** cFlag $= 1$; **exit**

        end for

        if(cFlag $= 0$ and $k = k_{\max}$)**then** show error information

        else if(cFlag$=0$)**then cycle**

        else if(cFalg$=1$)**then**

          (a) find $(\xi_{\mathrm{c}}^1, \xi_{\mathrm{c}}^2)$ at the projection via the Brent iteration

          (b) compute contact force and add it to current DE

          (c) compute the distribution and add it to nodes

    end loop

end loop

21

Because of the C_0 continuity nature of a FE mesh surface, a DE/FE contact method may have to deal with several distinct contact cases: DE-surface, DE-edge and/or DE-node contact [11, 15, 16, 60], and thus may lead to the time discontinuity of the contact force. The IGA/DEM method proposed here, however, only needs to handle the the contact problem between DEs and smooth NURBS surfaces. As a result, the contact forces are always time-continuous, if ignoring contacts between DEs and sharp corners or C_0 edges of a NURBS patch or patches.

5. Numerical examples

In order to assess the accuracy and robustness of the proposed coupling method, three examples involving contact between DEs and NURBS surfaces are simulated. The first two examples are mainly employed to examine the accuracy of the method. In these two examples, the bonded DEM model which is appropriate for analyzing elastic and brittle materials, is used in the DEM domain. In order to investigate the robustness of the proposed algorithm, the DEM contact model is employed to model the granular materials in the third example. In all these examples, the interaction between the DE domain and the IGA domain is handled by using the proposed approach based on the penalty function method where the penalty factor γ is selected to avoid large penetrations or oscillations between the DEM and IGA domains. In addition, the critical time step of the central difference method is the smallest among those determined by DEs, IGA elements and the DEM/IGA interactions. The time steps used in the these examples are all much smaller than the corresponding critical time steps.

5.1. Impact between double symmetric bars

Because its analytical solution is available, the impact problem of double symmetric bars in elastic range is often used to test numerical contact methods [15, 61, 62]. Herein, this impact process is also considered to assess the proposed coupling method in elastic range. The geometry, material constants and initial conditions of the impact system are listed in Table 2. At the beginning of the impact, the two bars with no constraint have a gap of 0.5 mm between their closed ends and move towards each other with an initial relative velocity of 20 m/s.

In the simulation, the right bar is analyzed using IGA, while the left bar is modeled by the bonded DEM, as shown in Fig. 12. The DEM region contains

22

10000 bonded discrete elements with a radius of 0.25 mm, and the IGA region is divided into 332 equal-sized IGA elements of degree two. The interaction between both DEM and IGA regions is dealt with by the IGA/DEM coupling approach proposed. The nominal Young's modulus for contact is set as

$$E_c = \min\{E_i/(1 - 2\nu_i), E_d/(1 - 2\nu_d)\}$$

where E_i and ν_i are the Young's modulus and Poisson's ratio of the IGA domain respectively, while E_d and ν_d are those of the DEM domain. To calculate the internal forces of IGA elements, the Gauss integration is employed with three points in each direction of the parameter space. The time step used in the central difference method is chosen to be 10^{-5} ms.
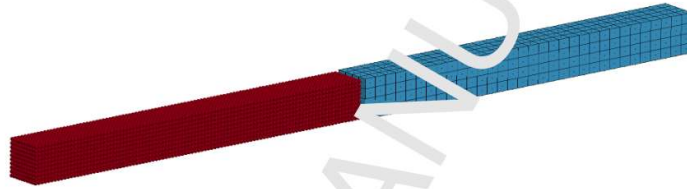
Figure 12: IGA/DEM model of two symmetric bars

Table 2: The geometry, initial velocity and material properties of the twin-bar system

Length of the bars	50 mm
Cross section of the bars	5 mm × 5 mm
Initial gap between the bars	0.5 mm
Initial relative velocity of the bars	20 m/s
Radius of DEs	0.25 mm
Mass density of the bars	10^{-3} g/mm^3
Young's modulus of the bars	1.0 GPa
Poisson's ratio of the bars	0.0

Because the penalty function method is employed to handle the interaction between the DEM and IGA regions in the coupling approach, the penalty factor has a direct influence on computational results. Thus, different penalty factors are chosen to observe the influence. The time histories of the contact-force, velocity and displacement at the free ends computed with different penalty factors are compared with the analytical solutions and

23

displayed in Figs. 13, 14 and 15. The results show that the numerical results are generally in good agreement with the analytical solutions, but fluctuate around the analytical solutions, particularly at the beginning of the impact. The figures also demonstrate that the numerical results with larger penalty factors tend to agree better with the analytical solutions, while at the same time the contact force and velocity fluctuate more severely. Thus, the penalty factor is usually chosen to be sufficiently large with acceptable fluctuations. This confirms the general behaviour of the penalty function method in the explicit FEM and DEM/FEM coupling method.
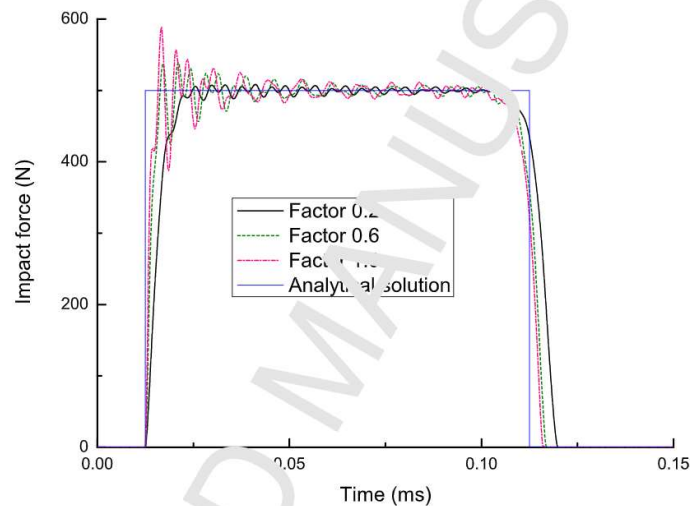
Figure 13: Comparison of the time histories of the contact-force with different penalty factors

5.2. A tube impacting a strip footing

In the above example, some features of the proposed coupling method have been demonstrated and its validity and accuracy to handle the collision with small deformation at the contact area has also been tested. To further test the ability of the proposed method to handle the collision with relatively large deformation, a tube impacting a strip footing with an initial velocity of 10 m/s is considered as shown in Fig. 16 and Table 3.

In the DEM/FEM coupling model as shown in Fig. 17, the strip footing with a fixed bottom surface is analyzed by the bonded DEM, and the tube is simulated by IGA. The open knot vectors are employed not only in the axial
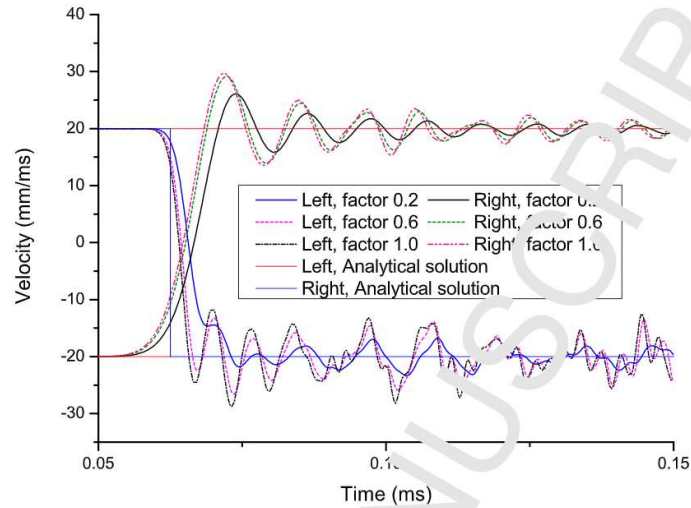
24

Figure 14: Comparison of the time histories of the velocity at the free ends with different penalty factors
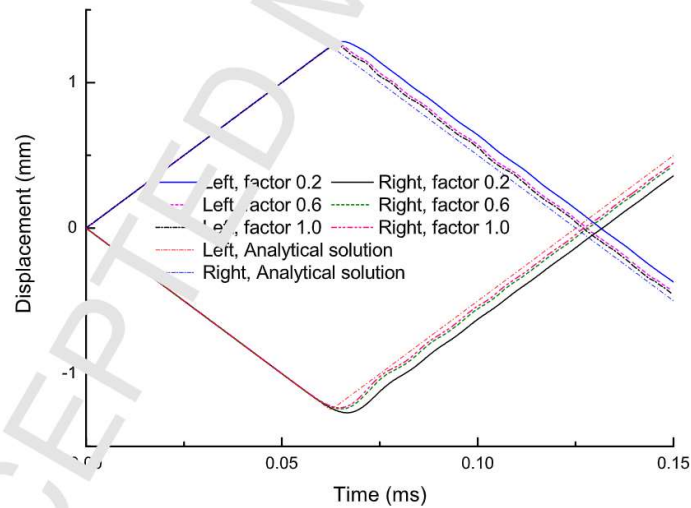

Figure 15: Comparison of the time histories of the displacement at the free ends with different penalty factors

25

and radial directions but also in the circumferential direction of the tube. Thus, there is a zero-thickness opening along its axial and radial directions in the tube IGA model, as shown in Fig. 17. In order to model the physical continuity of the tube, a penalty function method is employed to prevent the separation and penetration of the free surface on the tube opening.

In the simulation, the nominal Young's modulus for contact is calculated the same as that in Section 5.1, and the penalty factor η for the IGA/DEM contact force is set to be 0.12. For comparison, the same penalty function and factor are used to model contacts in the corresponding FE model. The time step for both models is set to be 10^{-5} ms.
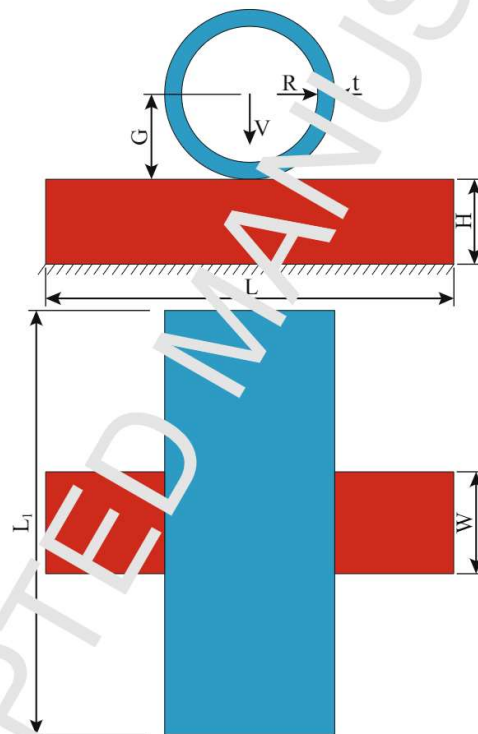
Figure 16: The geometry of the tube-strip impact system

The time histories of the contact-force and the displacement at points A and B (depicted in Fig. 17) are shown in Figs. 18 and 19, respectively. These figures illustrate that the results obtained from the proposed coupling method agree reasonably well with those calculated by FEM. In Fig. 19, the
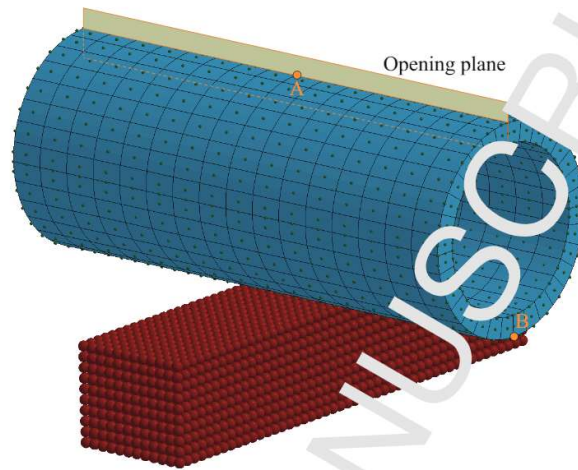
26

Figure 17: The IGA/DEM coupling model of the tube-strip impact system

Table 3: Geometry, initial velocity and material properties of the tube-strip impact system

Dimensions of the strip, $L \times W \times H$	$48 \times 12 \times 10$ mm
Dimensions of the tube, $R \times L_1 \times t$	$8 \times 28 \times 2$ mm
Initial position of the tube, G	5.0 mm
Initial velocity of the tube, V	10 m/s
Radius of DEs, r	0.5 mm
Mass density of the tube and strip, ρ	10^{-3} g/mm^3
Young's modulus of the tube and strip, E	1.0 GPa
Poisson's ratio of the tube and strip, ν	0.0

27
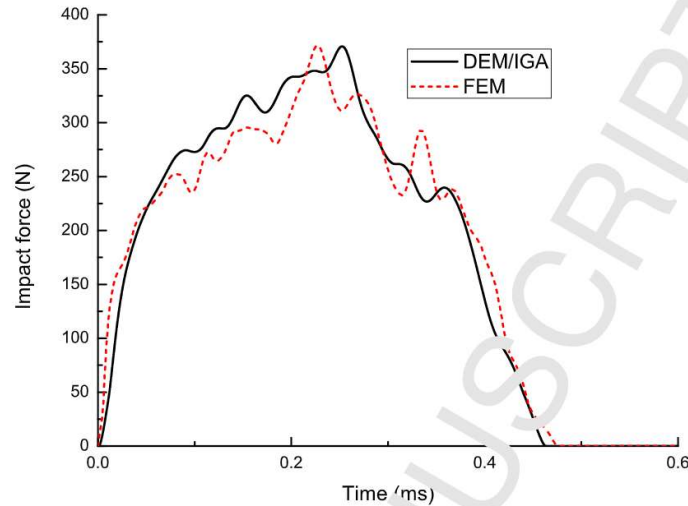
Figure 18: Comparison of the contact-force histories

displacement along the impact direction at point A tends to be larger than that at point B, mainly because the inertia force near point A is larger than that near point B at the time around 0.2 ms. In addition, since the penalty function method is used to prevent the separation and penetration of the tube opening in the IGA model, the displacement difference between the FEM and the proposed approach at point A is slightly larger than that at point B.

At time instants t= 0.2 ms and 0.4 ms, the displacement distributions from the IGA/DEM coupling model are compared with those from the FEM model as shown in Figs. 20 and 21, and they are generally in good agreement despite of some fine discrepancy.

No direct comparison in terms of the overall computational efficiency is made between the IGA/DEM and the FEM/DEM. It is obvious that the computation involved in the contact between a DE and an IGA element is higher than that between a DE and an FE element. Nevertheless, a very small number of IGA elements is required to accurately represent the geometry of the structure. Also the IGA representation leads to smooth contact surfaces. Hence, the contact force for every contact pair in the proposed IGA/DEM method is continuous with time. These are, however, difficult to be achieved by using the coupling FEM/DEM method because of the non-smoothness connection between neighbouring FE surfaces.
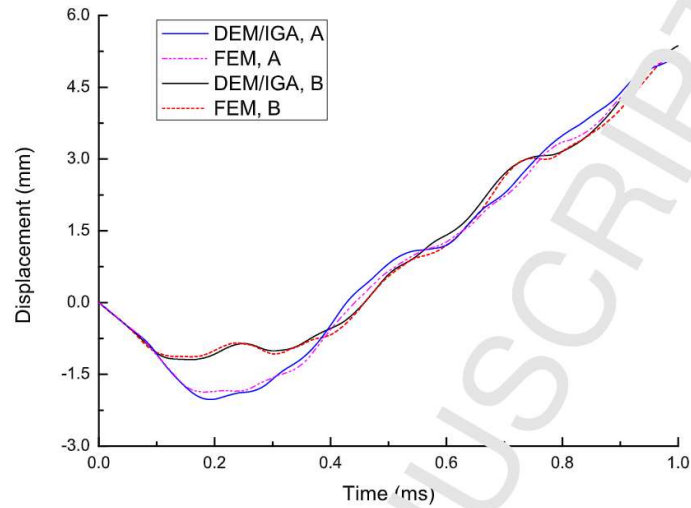
28

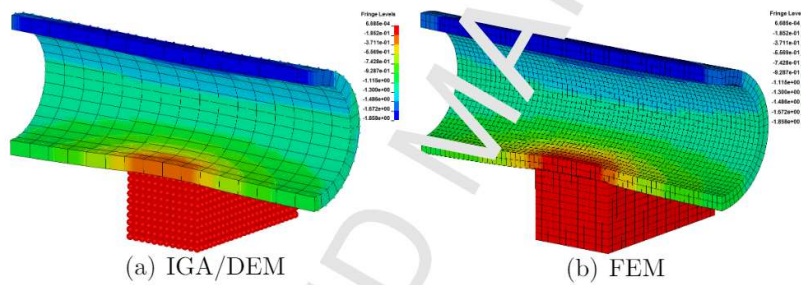Figure 19: Comparison of the displacement histories at points A and B on the tube surface

(a) IGA/DEM

(b) FEM

Figure 20: Comparison of the displacement distributions in the vertical direction at 0.2 ms
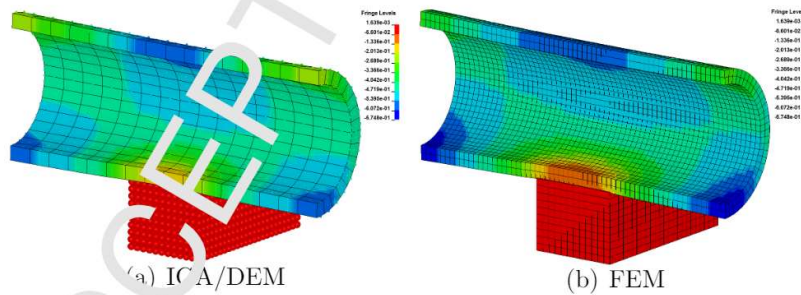

(a) IGA/DEM

(b) FEM

Figure 21: Comparison of the displacement distributions in the vertical direction at 0.4 ms

29

5.3. Granules impacting tailor rolled blank

To further test the applicability of the IGA/DEM coupling approach proposed, granules impacting a tailor rolled blank (TRB) is considered as shown in Fig. 22. At the beginning, 6144 particles with a radius of 0.5 mm move toward the TRB with an initial velocity of 10.0 m/s, and the particles at the bottom are just in contact with the wave crest of the top surface of the TRB. The material constants of the particles and the TRB are depicted in Table 4. The particles are modeled as DEs and the TRB is modeled by 1332 second-degree solid elements of IGA.

The contact between the DEs and the IGA elements is handled with the proposed coupling method. However, the classic Hertz model, namely Eq. (18), is adopted to calculate the normal contact force between a DE and an IGA element. This is based on a further investigation [63] which shows that the Hertz model without the penalty factor correction is the best normal contact interaction law between a spherical DE and a deformable structural element. The time step used in the central difference method is set to be 10^{-5} ms.
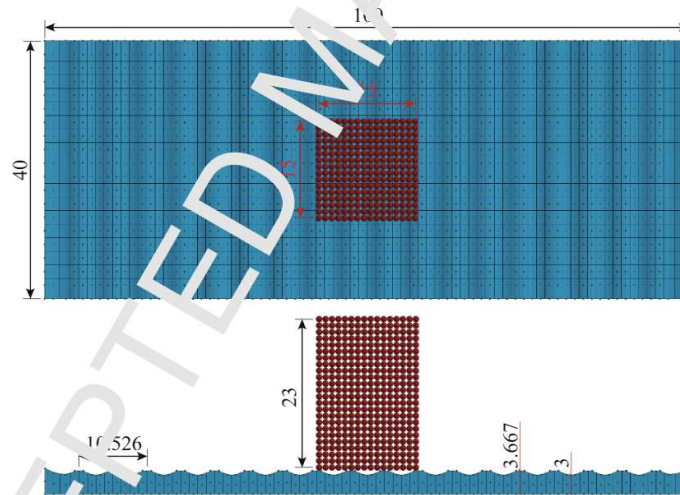

Figure 22: The geometry of the granules impacting TRB system (unit: mm)

Both impact force and displacement histories in the vertical direction at the center of the TRB bottom surface are displayed in Fig. 23. From 0 ms to 0.5 ms the impact force first increases and then decreases. In the following

30

Table 4: Radius, initial velocity of particles, and material properties of particles and TRB

Initial velocity of the particles, V	10.0 m/s
Particle's radius, r	0.5 mm
Mass density of the particles and TRB, ρ	10⁻³ g/mm³
Young's modulus of the particles and TRB, E	1.0 GPa
Poisson's ratio of the particles and TRB, ν	0.0

time interval [0.5, 0.65]ms, the impact force remains near zero, and most particles seem to not maintain contact with the TRB during this time period. Afterwards, some particles and TRB are in contact again, and thus the impact force starts to increase. Because most particles move upwards, the impact force tends to be relatively small. From 0 ms to 0.83 ms, the displacement increases in the impact direction and the TRB absorbs impact energy that is mainly transferred to strain energy. After 0.83 ms, the TRB begins to release strain energy and the displacement along the impact direction begins to decline.

The configurations of the particles and the velocity distributions are displayed in Fig. 24 at four different time instants. As the particles move down, some bottom particles are in contact with the crest area of the TRB top surface first and the velocities of the particles in these columns begin to decrease as shown in Fig. 24(a). Then, more particles at the bottom come to be in contact with the TRB top surface as shown in Fig. 24(b). Afterwards, in Figs. 24(c) and (d) the particles scatter mainly along the longitudinal direction because of the fluctuation of the TRB top surface in this direction. As shown in Fig. 24, the velocity distributions of the particles and the TRB are roughly symmetrical along the width and length directions because of the symmetry of the model in these directions. Furthermore, no large penetration is observed between the particles and the TRB.

6. Conclusions

A three-dimensional isogeometric/discrete-element method has been presented to take the advantages of the geometry smoothness and exactness in isogeometric analysis and the neighboring element interaction flexibility in discrete element modelling. In the coupling phase, candidate contact pairs are detected by modifying the CGRID method, and the exact contact position is found by modifying the simplex and Brent iterations in the local
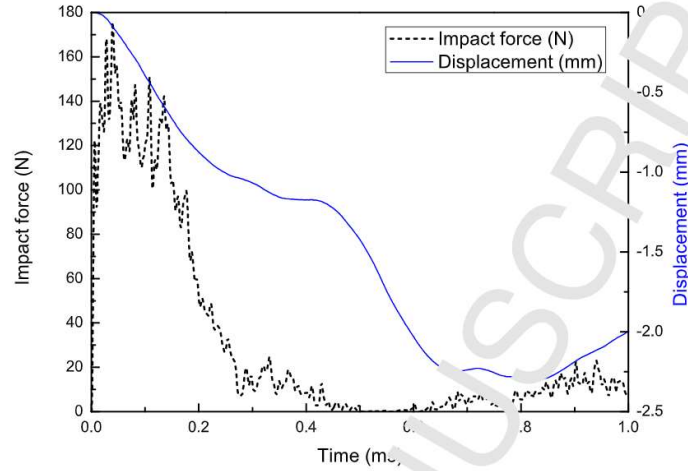
31

Figure 23: The impact force displacement histories at the center of the TRB bottom surface
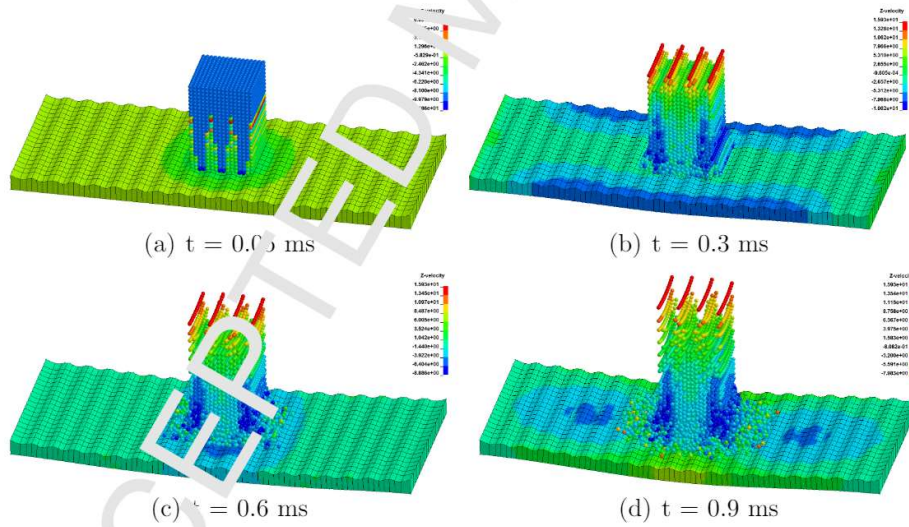

(a) t = 0.0 ms

(b) t = 0.3 ms

(c) t = 0.6 ms

(d) t = 0.9 ms

Figure 24: The velocity distributions in the vertical direction and the particle configurations at four time instants

32

search. The contact force between IGA and DEM is determined by a nonlinear penalty function based method, and it is found that the penalty factor should be set sufficiently large but without causing severe fluctuations in the results. Furthermore, a coupled IGA/DEM program CICADEM has been developed. The accuracy of numerical solutions of the two examples based on the 3D coupling model has been assessed in elastic regime by comparison with the corresponding analytical solution and/or a FEM model. The applicability of the coupling approach for modeling granular particle impact on a tailor rolled blank has also been tested.

The overall computational efficiency of the proposed IGA/DEM method is lower compared to the conventional FEM/DEM scheme as the computation involved in the DE/IGA contact is higher that of the DE/FEM contact. However, the geometric exactness and smoothness of IGA representations offers the feature that the contact force between a DE/IGA contact pair is always time-continuous, which cannot be matched by a DE/FE contact pair. Thus, unless having a well-defined set of comparison criteria, a fair comparison between the IGA/DEM and the FEM/DEM is difficult to be quantified. For this reason, no direct comparison of the computational efficiency between the two methods has been made in the numerical examples presented.

In the current work, friction between IGA elements and discrete elements has not been considered, but can be included within the current coupling framework.

Acknowledgment

References

[1] Munjiza A A, Knight EE, Rougier E. Computational mechanics of discontinua. John Wiley & Sons; 2011.

[2] Cundal PA. A computer model for simulating processive, large-scale movement in block rock system. In: Proceedings of the International

33

Symposium on Rock Mechanics, 1971. Symp ISRM Proc, Nancy, France; 1971, p. 129–39.

[3] Cundall PA, Strack OD. A discrete numerical model for granular assemblies. Geotechnique 1979;29(1):47–65.

[4] Potyondy DO, Cundall P. A bonded-particle model for rock. International journal of rock mechanics and mining sciences 2004;41(8):1329–64.

[5] Gao W, Liu L, Liao Z, Chen S, Zang M, Tan Y. Discrete element analysis of the particle mixing performance in a ribbon mixer with a double u-shaped vessel. Granular Matter 2019;21(1):13. doi:10.1007/s10035-018-0864-4.

[6] Han K, Peric D, Owen D, Yu J. A combined finite/discrete element simulation of shot peening processes-part II: 3D interaction laws. Engineering Computations 2000;17(6):680–702.

[7] Munjiza AA. The combined finite-discrete element method. John Wiley & Sons, England; 2004.

[8] Owen D, Feng Y, de Souza Neto E, Cottrell M, Wang F, Andrade Pires F, et al. The modelling of multi-fracturing solids and particulate media. International Journal for Numerical Methods in Engineering 2004;60(1):317–39.

[9] Onate E, Rojek J. Combination of discrete element and finite element methods for dynamic analysis of geomechanics problems. Computer methods in applied mechanics and engineering 2004;193(27-29):3087–128.

[10] Xiang J, Munjiza A, Latham JP. Finite strain, finite rotation quadratic tetrahedral element for the combined finite–discrete element method. International journal for numerical methods in engineering 2009;76(8):946–78.

[11] Zang M, Gao W, Lei Z. A contact algorithm for 3D discrete and finite element contact problems based on penalty function method. Computational Mechanics 2011;48(5):541–50.

34

[12] Dang HK, Meguid MA. An efficient finite-discrete element method for quasi-static nonlinear soil-structure interaction problems. International Journal for Numerical and Analytical Methods in Geomechanics 2013;37(2):130–49.

[13] Tran V, Meguid M, Chouinard L. A finite-discrete element framework for the 3D modeling of geogrid-soil interaction under pullout loading conditions. Geotextiles and Geomembranes 2013;37:1–9.

[14] Hu L, Hu G, Fang Z, Zhang Y. A new algorithm for contact detection between spherical particle and triangulated mesh boundary in discrete element method simulations. International Journal for Numerical Methods in Engineering 2013;94(8):787–804.

[15] Chen H, Zhang Y, Zang M, Hazell PJ. An accurate and robust contact detection algorithm for particle-solid interaction in combined finite-discrete element analysis. International Journal for Numerical Methods in Engineering 2015;103(8):598–624.

[16] Gao W, Tan Y, Jiang S, Zhang G, Zang M. A virtual-surface contact algorithm for the interaction between FE and spherical DE. Finite Elements in Analysis and Design 2016;108:32–40.

[17] Munjiza A, Knight EE, Rougier E. Large strain finite element method: a practical course. John Wiley & Sons; 2015.

[18] Wriggers P. Computational contact mechanics, 2nd edn. Springer-Verlag, Berlin; 2006.

[19] Santasusana M. Numerical techniques for non-linear analysis of structures combining discrete element and finite element methods. Ph.D. thesis; Polytechnic University of Catalonia; 2017.

[20] Feng Y, Owen D. A 2D polygon/polygon contact model: algorithmic aspects. Engineering Computations 2004;21(2/3/4):265–77.

[21] Feng YT, Han K, Owen DRJ. Energy-conserving contact interaction models for arbitrarily shaped discrete elements. Computer Methods in Applied Mechanics and Engineering 2012;205-208:169–77.

35

[22] Hughes TJ, Cottrell JA, Bazilevs Y. Isogeometric analysis: CAD, finite elements, NURBS, exact geometry and mesh refinement. Computer Methods in Applied Mechanics and Engineering 2005;194(39-41):4135–95.

[23] Cottrell JA, Hughes TJ, Bazilevs Y. Isogeometric analysis: toward integration of CAD and FEA. John Wiley & Sons, 2009.

[24] Cottrell JA, Reali A, Bazilevs Y, Hughes TJ. Isogeometric analysis of structural vibrations. Computer Methods in Applied Mechanics and Engineering 2006;195(41-43):5257–96.

[25] Phung-Van P, Tran LV, Ferreira A, Nguyen-Xuan H, Abdel-Wahab M. Nonlinear transient isogeometric analysis of smart piezoelectric functionally graded material plates based on generalized shear deformation theory under thermo-electro-mechanical loads. Nonlinear Dynamics 2017;87(2):879–94.

[26] Nguyen-Thanh N, Zhou K, Zhuang X, Areias P, Nguyen-Xuan H, Bazilevs Y, et al. Isogeometric analysis of large-deformation thin shells using RHT-splines for multiple patch coupling. Computer Methods in Applied Mechanics and Engineering 2017;316:1157–78.

[27] Guo Y, Heller J, Hughes TJ, Ruess M, Schillinger D. Variationally consistent isogeometric analysis of trimmed thin shells at finite deformations, based on the STEP exchange format. Computer Methods in Applied Mechanics and Engineering 2018;336:39–79.

[28] Kruse R, Nguyen-Thanh N, Wriggers P, De Lorenzis L. Isogeometric frictionless contact analysis with the third medium method. Computational Mechanics 2018;:1–13.

[29] Bazilevs Y, Pigazzini M, Ellison A, Kim H. A new multi-layer approach for progressive damage simulation in composite laminates based on isogeometric analysis and Kirchhoff-Love shells. Part I: basic theory and modeling of delamination and transverse shear. Computational Mechanics 2018;62(3):563–85.

[30] Peng X, Atroshchenko E, Kerfriden P, Bordas S. Isogeometric boundary element methods for three dimensional static fracture and fatigue

36

crack growth. Computer Methods in Applied Mechanics and Engineering 2017;316:151–85.

[31] Buffa A, Sangalli G, Vázquez R. Isogeometric methods for computational electromagnetics: B-spline and T-spline discretizations. Journal of Computational Physics 2014;257:1291–320.

[32] Takizawa K, Tezduyar TE, Otoguro Y, Terahara T, Kuraishi T, Hattori H. Turbocharger flow computations with the space–time isogeometric analysis (ST-IGA). Computers & Fluids 2017;142:15–20.

[33] Li W, Nguyen-Thanh N, Zhou K. Geometrically nonlinear analysis of thin-shell structures based on an isogeometric-meshfree coupling approach. Computer Methods in Applied Mechanics and Engineering 2018;336:111–34.

[34] Chasapi M, Klinkel S. A scaled boundary isogeometric formulation for the elasto-plastic analysis of solids in boundary representation. Computer Methods in Applied Mechanics and Engineering 2018;333:475–96.

[35] Chen L, Liu C, Zhao W, Liu L. An isogeometric approach of two dimensional acoustic design sensitivity analysis and topology optimization analysis for absorbing material distribution. Computer Methods in Applied Mechanics and Engineering 2018;336:507–32.

[36] Williams JR, Perkins E, Cook B. A contact algorithm for partitioning n arbitrary sized objects. Engineering Computations 2004;21(2/3/4):235–48.

[37] Han K, Feng Y, Owen D. Performance comparisons of tree-based and cell-based contact detection algorithms. Engineering Computations 2007;24(2):165–81.

[38] Moré JJ, Cosnard MY. Numerical solution of nonlinear equations. ACM Transactions on Mathematical Software (TOMS) 1979;5(1):64–85.

[39] Brent RP. Some efficient algorithms for solving systems of nonlinear equations. SIAM Journal on Numerical Analysis 1973;10(2):327–44.

37

[40] Kopaka J, Gabriel D, Pleek J, Ulbin M. Assessment of methods for computing the closest point projection, penetration, and gap functions in contact searching problems. International Journal for Numerical Methods in Engineering 2016;105(11):803–33.

[41] Temizer I, Wriggers P, Hughes T. Contact treatment in isogeometric analysis with NURBS. Computer Methods in Applied Mechanics and Engineering 2011;200(9-12):1100–12.

[42] Di Renzo A, Di Maio FP. Comparison of contact-force models for the simulation of collisions in DEM-based granular flow codes. Chemical Engineering Science 2004;59(3):525–41.

[43] Escotet-Espinoza MS, Foster CJ, Ierapetritou M. Discrete element modeling (DEM) for mixing of cohesive solids in rotating cylinders. Powder Technology 2018;335:124–36.

[44] Zang M, Lei Z, Wang S. Investigation of impact fracture behavior of automobile laminated glass by 3D discrete element method. Computational Mechanics 2007;41(1):73–83.

[45] Gao W, Zang M. The simulation of laminated glass beam impact problem by developing fracture model of spherical DEM. Engineering Analysis with Boundary Elements 2014;42:2–7.

[46] Wang M, Feng Y, Wang C. Numerical investigation of initiation and propagation of hydraulic fracture using the coupled Bonded Particle–Lattice Boltzmann Method. Computers & Structures 2017;181:32–40.

[47] Johnson KL, Johnson KL. Contact mechanics. Cambridge University Press; 1987.

[48] Griffiths D, Mustoe GG. Modelling of elastic continua using a grillage of structural elements based on discrete element concepts. International Journal for Numerical Methods in Engineering 2001;50(7):1759–75.

[49] Kaixin L, Lingtian G. The application of discrete element method in solving three-dimensional impact dynamics problems. Acta Mechanica Sonida Sinica 2003;16(3):256–61.

38

[50] Liu K, Liu W. Application of discrete element method for continuum dynamic problems. Archive of Applied Mechanics 2006;75(3-4):229–43.

[51] Gao W, Tan Y, Zang M. A cubic arranged spherical discrete element model. International Journal of Computational Methods 2014;11(05):1350102.

[52] Feng Y, Owen D. An augmented spatial digital tree algorithm for contact detection in computational mechanics. International Journal for Numerical Methods in Engineering 2002;55(2):159–76.

[53] Matzen M, Cichosz T, Bischoff M. A point to segment contact formulation for isogeometric, NURBS based finite elements. Computer Methods in Applied Mechanics and Engineering 2013;255:27–39.

[54] De Lorenzis L, Temizer I, Wriggers P, Zavarise G. A large deformation frictional contact formulation using NURBS-based isogeometric analysis. International Journal for Numerical Methods in Engineering 2011;87(13):1278–300.

[55] Dimitri R, De Lorenzis L, Scott M, Wriggers P, Taylor R, Zavarise G. Isogeometric large deformation frictionless contact using T-splines. Computer methods in applied mechanics and engineering 2014;269:394–414.

[56] De Lorenzis L, Wriggers P, Zavarise G. A mortar formulation for 3d large deformation contact using NURBS-based isogeometric analysis and the augmented Lagrangian method. Computational Mechanics 2012;49(1):1–20.

[57] Kim JY, Youn SK. Isogeometric contact analysis using mortar method. International Journal for Numerical Methods in Engineering 2012;89(12):1559–81.

[58] De Lorenzis L, Wriggers P, Hughes TJ. Isogeometric contact: a review. GAMM-Mitteilungen 2014;37(1):85–123.

[59] Spendley W, Hext GR, Himsworth FR. Sequential application of simplex designs in optimisation and evolutionary operation. Technometrics 1962;4(4):441–61.

[60] Zheng Z, Zang M, Chen S, Zhao C. An improved 3D DEM-FEM contact detection algorithm for the interaction simulations between particles and structures. Powder Technology 2017;305:308–22.

[61] Laursen T, Chawla V. Design of energy conserving algorithms for frictionless dynamic contact problems. International Journal for Numerical Methods in Engineering 1997;40(5):863–86.

[62] Armero F, Petőcz E. Formulation and analysis of conserving algorithms for frictionless dynamic contact/impact problems. Computer Methods in Applied Mechanics and Engineering 1998;158(3-4):269–300.

[63] Gao W, Feng Y. A coupled 3D discrete elements/iso-geometric method for particle/structure interaction problems; 2019. (in press).

40